Experimental Thermal and Fluid Science 142 (2023) 110823

Contents lists available at ScienceDirect

Experimental Thermal and Fluid Science

journal homepage: www.elsevier.com/locate/etfs

An experimental study of dynamic icing process on an Aluminum-Conductor-Steel-Reinforced power cable with twisted outer strands

Ramsankar Veerakumar [1], Linchuan Tian, Haiyang Hu, Yang Liu, Hui Hu [*]

Dept. of Aerospace Engineering, Iowa State University, Ames, IA 50011-2271, USA

ARTICLE INFO

Keywords:
Aluminum-Conductor-Steel-Reinforced (ACSR) cable
Power cable icing physics
Aerodynamic drag of iced cables
Quantification of 3D shapes of accreted ice structures

ABSTRACT

An experimental campaign was conducted to investigate the dynamic icing process on an Aluminum-Conductor-Steel-Reinforced (ACSR) power cable with twisted outer strands and characterize the resultant wind loads experienced by the power cable under both dry rime and wet glaze icing conditions. In addition to recording the dynamic icing process over the cable surface with a high-resolution imaging system, the three-dimensional (3D) shapes of the ice layers accreted on the cable model were also quantified by using a novel 3D profile scanning system. While the evolution of the wake flow behind the iced ACSR cable was quantified with a Particle Image Velocimetry (PIV) system, the variation of the wind loads experienced by the cable model was also examined based on the measurements of force/moment transducers. Under the dry rime icing condition, opaque, grainy ice was found to accrete only within the impinging zone of airborne water droplets over the cable frontal surface without any noticeable water runback flow over the cable surface. In comparison, substantial unfrozen water was observed to run back over the cable surface under the wet glaze icing condition, causing the formation of transparent, glazy ice layer over a much wider area over the cable surface. Correlating with the formation of more complicated glazy ice humps/horns over the ACSR cable surface, the accumulated ice mass was found to grow much faster during glaze icing process, in comparison to that of rime icing case. While the resultant wind loads acting on the iced ACSR cable was found to decrease gradually with the increasing icing time under the rime icing condition, the corresponding values were found to increase continuously under the glaze icing condition.

1. Introduction

Electrical power transmission cable icing is a well-known problem for people living in cold climate. Power cable icing has been reported to degrade the power network reliability greatly. In extreme conditions, the atmospheric icing could result in significant damages to electrical power distribution networks, causing long term power disruption [1–4]. The importance of effective icing control for power transmission cables is highlighted by a number of catastrophic incidents/accidents in recent years. For example, a major icing storm in Ontario and Quebec, Canada in winter of 1998 caused loss of power to about one million customers with a duration of 3–30 days. Since several miles of transmission and distribution cables were destroyed, the cost was estimated to be over one billion Canadian dollars for reconstructing the damaged power cables along with a social cost due to the incident exceeding 3.0 times of the estimated cost [5].

Ice accretion characteristics on power cables are of great important to predict the potential risks. It was found that the variations in shape, density, and size of the accreted ice layers would affect the wind loads experienced by the power cables significantly. While the accreted ice weight would increase the vertical loads experienced by the power cables and the supporting structures, the combined effects of wind and ice may result in transverse loads increasing significantly. It may also induce significant vibrational loads, especially when the ice depositions over the cable surfaces are asymmetric [6]. Wind-induced-vibrations (the vibrations induced by unsteady vortex shedding) are known to cause detrimental effects on the durability and reliability of the cables and related components. Damping devices are usually used to mitigate

* Corresponding author.
E-mail address: huhui@iastate.edu (H. Hu).
[1] Current address: Dept. of Mechanical Engineering, University of Wyoming, Laramie 82072, USA.

https://doi.org/10.1016/j.expthermflusci.2022.110823
Received 24 July 2022; Received in revised form 9 October 2022; Accepted 28 November 2022
Available online 1 December 2022

these vibrations. The situation can change dramatically when ice accretes on the power transmission cables since the vibrations of iced cables may occur outside the design frequency of the dampers. Galloping, which is another kind of wind-induced instability to cause low frequency, large amplitudes vibrations, can also occur on iced power cables [7]. Furthermore, power cable icing may also cause flashover, in which power transmission cables would be in motion due to lift forces induced by icing and come in contact to cause unwanted electrical discharges between them. This may also happen as accreted ice chucks shed from the cables, resulting in sudden vertical motion [8–10].

Advancing of technology for safer and more efficient operation of power transmission cables under atmospheric icing conditions requires the development of innovative, effective anti-/de-icing strategies. Doing so requires a keen understanding of the underlying physics pertinent to the dynamic icing process over the surface of power transmission cables and the resultant wind loads induced by the ice accretion. While several numerical and experimental investigations have been conducted in recent years to study power transmission cable icing phenomena [11–16], most of them focused on characterizing the global features of the icing process, like providing measurement data for the validation of ice morphogenetic models, quantifying variations of the accumulated ice mass with the cable diameter, and estimating the maximum loads caused by wet snow/ice accumulated on power cables. Little can be found in literature to quantify the dynamic ice accretion process and characterize the evolution of the shapes of the ice layers accreted on power cables under different icing conditions. It should also be noted that almost all the previous studies were conducted with the power transmission cables being simplified as cylindrical test models with smooth cable surfaces. However, in reality, Aluminum-Conductor-Steel-Reinforced (ACSR in short) cables/conductors with rather rough, twisted outer strands are the most commonly used cables for overhead power transmission in primary and secondary distribution networks. In comparison to the ice accretion over smooth surfaces of simplified, cylindrical cable models, the influences of the rough, twisted outer strands of the ACSR cables on the icing characteristics under different icing conditions have not been well studied.

In the present study, an experimental campaign was conducted to investigate the dynamic icing process over the surface of an ACSR cable model and to examine the variations of the wind loads acting on the iced cable model during the dynamic icing process. A section of an ACSR power transmission cable, which is typically utilized for high-voltage electrical power transmission, was used as the test model in the present study. The ACSR cable model was mounted horizontally in an icing research tunnel under typical wet glaze and dry rime icing conditions. While the dynamic icing process on the cable surface was recorded with a high-resolution imaging system, the three-dimensional (3D) shapes of the iced cable model were characterized with a 3D profiler scanning system. Meanwhile, the wake characteristics behind the iced cable model were quantified with a digital Particle Image Velocimetry (PIV) system, the resultant wind loads experienced by the iced cable model were also measured by using a pair of high-sensitive moment/force transducers. The primary objective of the presents study is to characterize the effects of the rough, twisted outer strands wrapping around the ACSR cable on the dynamic icing process over the cable surface and the resultant wind loads acting the ACSR cable model, in comparing to those of simplified power cable model with smooth surface under the same icing conditions as reported in the published literature [21].

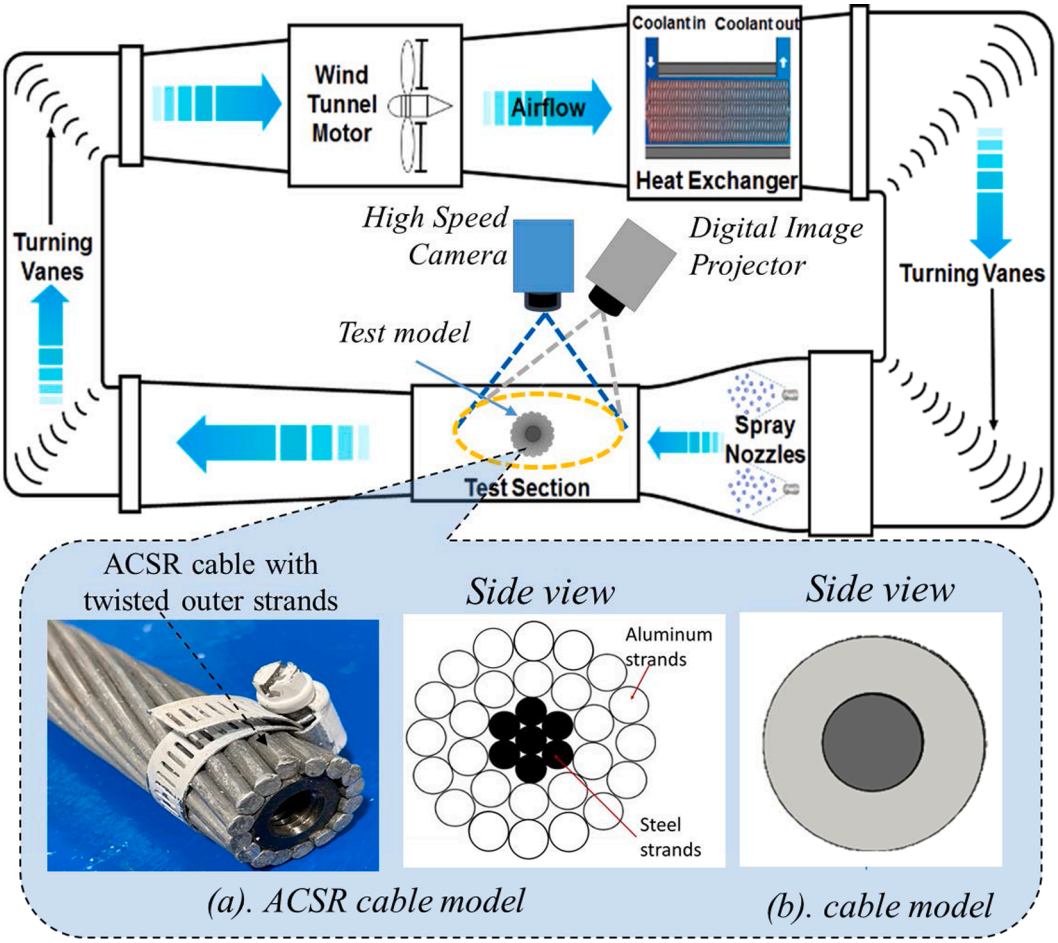

Fig. 1. ISU-IRT and the ACSR cable model.

2. Experimental setup and measurement systems

2.1. Icing research tunnel and ACSR cable model

The experimental investigation was performed in an Icing Research Tunnel available at Iowa State University (i.e., ISU-IRT in short). The test section of ISU-IRT is optically transparent with the dimension of 2.0 m (length) × 0.4 m (width) × 0.4 m (height). As shown schematically in Fig. 1, a 30-hp motor (Baldor™) was used to drive airflow circulating inside the tunnel with the airflow velocity up to 60 m/s. With a bell-shaped contraction section with a large area ratio of 10:1 was installed upstream of the test section to ensure smooth and uniform airstreams flowing into the test section of ISU-IRT. The turbulence intensity level of the incoming airflow in the test section was found to be within 2.0 %, as measured by using a hotwire anemometry system. With a refrigeration system powered by a 40-hp compressor (Vilter™), the airflow inside the ISU-IRT can be cooled down to −25 °C. A feedback control system was used to maintain the airflow at the desired testing temperature with the fluctuations within ± 0.5 °C. An array of eight spray nozzle/atomizers (IKEUCHI BIMV 8002) were mounted inside the ISU-IRT to inject tiny water droplets into the airflow. Based on the measurement results of a LaVision's *ParticleMaster™* system, the water droplets exhausted from the spray nozzles/atomizers were found to range from 10 μm to 100 μm in size with the mean-volume-diameter (MVD) being about 20 μm. By manipulating the flowrate of water flow supplied to the spray nozzles, liquid water content (LWC) level of the airflow inside ISU-IRT can be adjusted from 0.1 g/m^3 to 5.0 g/m^3. The ISU-IRT has been used to study various atmospheric icing phenomena over a wide range of icing conditions [17–21].

A section taken of the most-commonly-used ACSR power transmission cable provided by a local electric power company was selected as the test model in the present study. The ACSR cable model has an outer diameter of 29 mm with the span length of 400 mm. As illustrated in Fig. 1, the ACSR cable model has sixteen twisted aluminum outer strands with the diameter of each strand being 4.7 mm. With the twisted outer strands wrapping around the cable surface, the ACSR cable has a much rougher surface, in comparison to simplified, cylindrical cable models used in previous studies (i.e., the simplified cable model shown schematically in Fig. 1b). Sessile water droplets were found to have a contact angle of about 65° on the ACSR cable surface, indicating that the hydrophilic nature of the ACSR cable surface, which is found to agree well with the surface wettability of ACSR power cables reported in the literature [22].

2.2. Selection of the parameters for experiments

Ice accretion over a structural surface may be categorized as *rime*, *glaze,* or *mixed icing*, depending on the conditions under which the icing event occurs [23–25]. If the ambient temperature is relatively low (i.e., typically below −8.0 °C) and the incoming airflow is relatively dry (i.e., Liquid Water Content, $LWC \leq 1.0$ g/m^3), the airborne supercooled water droplets would freeze immediately as impacting onto the structural surface, forming *rime ice*. At relatively warmer temperatures just below the water freezing temperature (typically above −8.0 °C) with relatively high *LWC* levels of the incoming airflow ($LWC > 1.0$ g/m^3), the impinging supercooled droplets would be frozen partially with the rest of the impacted water droplets in liquid phase running back along structural surface. The runback water was frozen into ice later at further downstream locations, forming *glaze ice* with more complex ice shapes. *Mixed icing* refers the situation with simultaneous appearance of both *rime* and *glaze* icing characteristics.

In the present study, the incoming airflow speed was set at $V_\infty = 20$ m/s (i.e., the typically wind speed experienced by power cables in icing events) with the corresponding Reynolds number of the test model being $Re_D \approx 50{,}000$. Both *glaze* and *rime* icing events were simulated. Based on the results reported in literatures [21,26–28], while the relevant parameters for a typical glaze icing process were selected as $LWC = 2.0$ g/m^3 and $T_\infty = -5.0$ °C, the corresponding valves were $LWC = 1.0$ g/m^3 and $T_\infty = -15.0$ °C for the rime icing experiment. The icing experiment duration was set at 1,000 s for all the test cases.

2.3. Characterization of the dynamic ice accretion process on the ACSR cable surface

A high-resolution digital camera (PCO Tech, Dimax Camera of 2 K pixels × 2 K pixels in resolution) with an optical lens (Nikon, 60 mm Nikkor 2.8D) was used to record the dynamic icing process on the ACSR cable. While the camera was positioned vertically above the test model with a distance about 1.2 m, low-flicker illumination for the image acquisition was provided with high-power, halogen lamps (AmScope, HL250-AS).

A 3D profiler scanning system was also used to measure the shapes of the iced cable model. The 3D profiler scanning system is based on a novel digital-image-projection (DIP) technology with a structured light triangulation principle [29]. An optical projector was used to project a digital image with known characteristics onto the surface of the object of interest (i.e., the iced cable in the present study). Due to the ice accretion on the cable surface, projected patterns would appear deformed when observed from any direction other than the projection axis. The 3D shapes of the iced cable model can be reconstructed via a comprehensive image processing procedure to calculate the displacement of the projected patterns in the acquired images of the iced cable in related to the reference images without any ice accretion on the cable surface. Further information about the technical basis and measurement procedure of the 3D profiler scanning system can be found in our recently published papers [29–31].

For the 3D profiler scanning, the field view was set to be at the midspan of the ACSR cable model with a measurement window size of 100 mm by 100 mm. Same as that described in Peng et al. [31], the 3D ice shape scanning was conducted with the iced ACSR cable model still inside the ISU-IR. During the 3D profiler scanning operation, the airflow in the ISU-IRT was paused with the ambient temperature being kept at frozen cold. It takes about 30 s to finish the scanning operation, the morphology changes of the accreted ice structures on the ACSR cable model due to the 3D profile scanning operation are believed to be small. It should be noted that, the same system was also used by Veerakumar et al.[21] to measure the shapes of 3D printed hemispherical roughness elements on a test plate for the measurement accuracy estimation. Based on the measurements of about 500 points around a given hemispherical roughness element with a nominal height of 8.0 mm, the measurement uncertainty of the 3D profiler scanning system was found to be about 150 μm, i.e., ~ 2.0 % of the targeted height of the measurements.

2.4. A digital Particle image Velocimetry (PIV) system to quantify the wake flow characteristics

A digital PIV system was used to quantify the evolution of the wake flow behind the ACSR cable model before and during the icing process. For the PIV measurements before starting icing experiments, incoming airflow was seeded with ~1 μm oil droplets using a smoke generator for the PIV measurements. The airborne super-cooled water droplets were used as the tracer particles for the PIV measurements after starting ice accretion experiments. It should be noted that, since the supercooled water droplets suspended in the incoming airflow were estimated to have a mean volume diameter (MVD) of approximately 20 μm, the corresponding Stokes number of the airborne water droplets was estimated to be about 1.0 (i.e., $St = \frac{\rho_p {d_p}^2 U}{18\mu D} \approx 1.0$, where ρ_p is the density of water droplets, d_p is droplet diameter, U is the droplet flying velocity, μ is the dynamic viscosity of air, and D is the diameter of the cable model [32]), indicating a reasonable dynamic response of the airborne water droplets to follow the incoming airflow. Laser sheet illumination for the

PIV measurements was provided by a double-pulsed Nd:YAG laser (Evergreen, Big Sky Laser, 200 mJ @ 532 nm with a frame rate of 15 Hz) along with a set of mirrors and lenses with the laser sheet thickness being about 1.0 mm in the measurement region. PIV images were acquired by using a high-resolution digital camera (i.e., 2048 pixels by 2048 pixels, PCO-Tech^{TM}) and a Nikon lens (focal length 60 mm). The timing for the laser illumination and PIV image acquisition wase synchronized by using a digital delay generator (Berkeley Nucleonics, Model 565) to set the time interval between each pair of successive PIV image acquisitions being 30 μs. A frame-to-frame cross-correlation technique was adopted to calculate the instantaneous flow velocity vectors from the acquired PIV images with an interrogation window size of 32 pixels × 32 pixels. An effective overlap of 50 % of the interrogation windows was employed for PIV image processing, resulting in a spatial resolution of about 1.50 mm × 1.50 mm for the PIV measurements. The commercial PIV image processing software package of LaVision FlowMaster^{TM} was used to derive the instantaneous flow velocity vectors from the acquired PIV images, and the uncertainty for instantaneous PIV results was estimated to be about 2.0 %.

2.5. Wind load measurements with moment/force transducers

The variations of the wind load acting on the ice accreting cable model was measured by using a pair high-sensitivity force/moment transducers (i.e., ATI-IA Mini 45) mounted at two ends of the cable model. The force/moment transducers are composed of foil strain gage bridges, which can measure the aerodynamic forces along three mutually perpendicular axes, and the moment about each axis. The precision of the force/moment transducer is ± 0.25 % of the full range (10 N). In the present study, the two force/moment transducers were synchronized via a 16-bit data acquisition system (NI USB-6218). The unsteady aerodynamic force acting on the test model were measured at a data acquisition rate of 2,000 Hz.

3. Experimental results and discussions

Before starting the experiments, the icing tunnel was operated at the desired frozen-cold temperature for about 30 min to enable the tunnel reaching thermal equilibrium before turning on the spray system. After turning on the spray system, tiny water droplets exhausted from the nozzles/atomizers would be cooled down rapidly to become supercooled water droplets. Upon impinging onto the model surface, the supercooled water droplets would be solidified to start icing process immediately. While the primary objective of the present study is to examine the characteristics of the dynamic icing process over the ACSR cable surface and the resultant wind loads acting on the cable model, the effects of the twisted outer strands wrapped around the ACSR cable model on the ice accretion process were also investigated by comparing the measurement results of the present study to those reported in Veerakumar et al. [21] by exposing a simplified cylindrical cable model (with no twisted outer strands) to the same icing conditions.

3.1. Characteristics of icing process over the ACSR cable surface under the rime icing condition

Fig. 2 presents typical ice accretion images to show the dynamic rime icing process on the ACSR cable surface with $LWC = 1.0$ g/ m^3, $T_\infty = -15$ ºC, and $V_\infty = 20$ m/s. The images were taken before (i.e., $t = 0$ s,) and after turning on the spray nozzles/atomizers. It can be observed that, at relatively low temperature of $T_\infty = -15$ ºC, since all the released latent heat of fusion associated with the solidification of the impinged water droplets can be dissipated efficiently via the strong convective/conductive heat transfer over the cable surface [27], all the impacted water droplets would be frozen into ice instantly. As a result, accreted ice was observed to be restricted within the direct impingement zone of the airborne droplets over the cable front surface without any noticeable traces of water runback on the cable surface. The accreted ice layer was opaque and milky-white with a grainy appearance, which are typical characteristics of rime icing process [27]. As the icing time progressed, the ice layer accreted over the cable front surface was found to become thicker and thicker, causing the twisted outer strands on the front cable surface being buried under the ice layer completely after about 400 s of the rime icing experiments.

The 3D profiler scanning results given in Fig. 3 can be used to characterize of the rime icing process more quantitatively. The outer profiles of the accreted ice layer at any cross sections can also be extracted from the 3D profile scanning results of the iced ACSR cable. While Fig. 4(a) presents the variations of the outer profiles of the iced ACSR cable model in the middle section as the icing time progresses, the outer profiles of the iced cable at five different spanwise location after undergoing 1,000 s of the rime icing experiments were given in Fig. 4(b).

As shown in Fig. 4(a), the accreted rime ice layer was restricted within the direct impinging zone of the airborne droplets with the azimuthal angular limits at $\theta_{upper\text{-}limit} \approx +80°$ and $\theta_{lower\text{-}limit} \approx -80°$. Similar to that reported in a previous study [33], the rime icing process would be influenced mainly by the droplet collection efficiency distribution over the cable frontal surface. Corresponding to the higher droplet collection efficiency near the cable leading edge [34], the ice layer accreted near the cable leading edge was found to be much thicker than those at further downstream locations. Thus, as the time

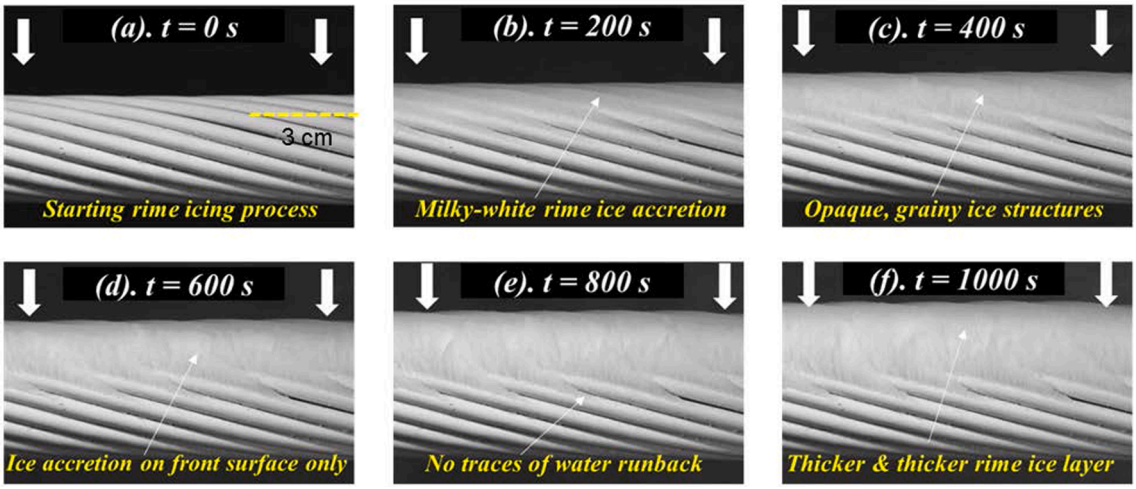

Fig. 2. Acquired images of the rime icing process over the ACSR cable surface.

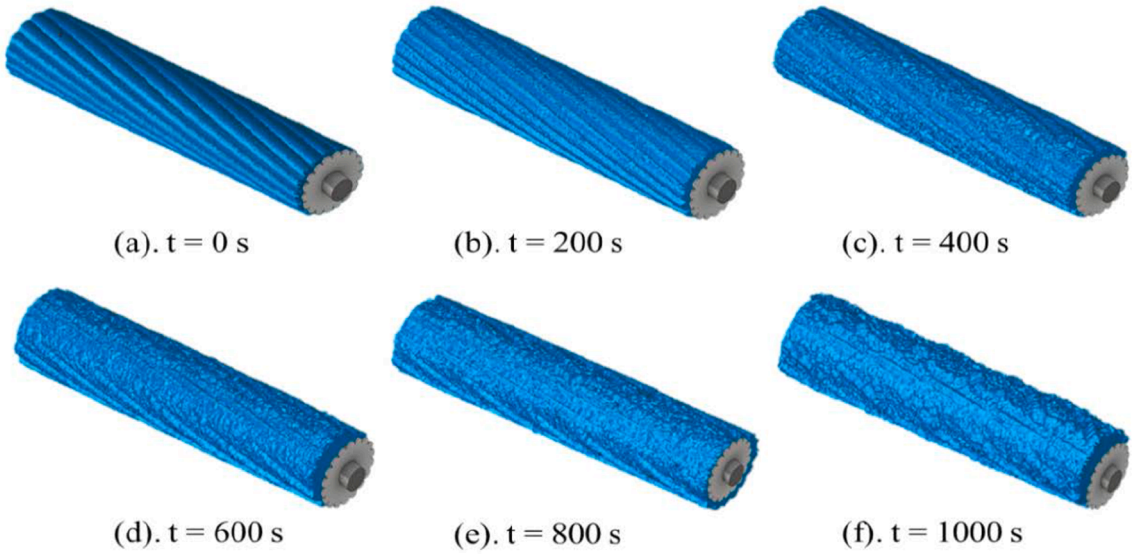

Fig. 3. Measured shapes of the iced ACSR cable model during the rime icing process.

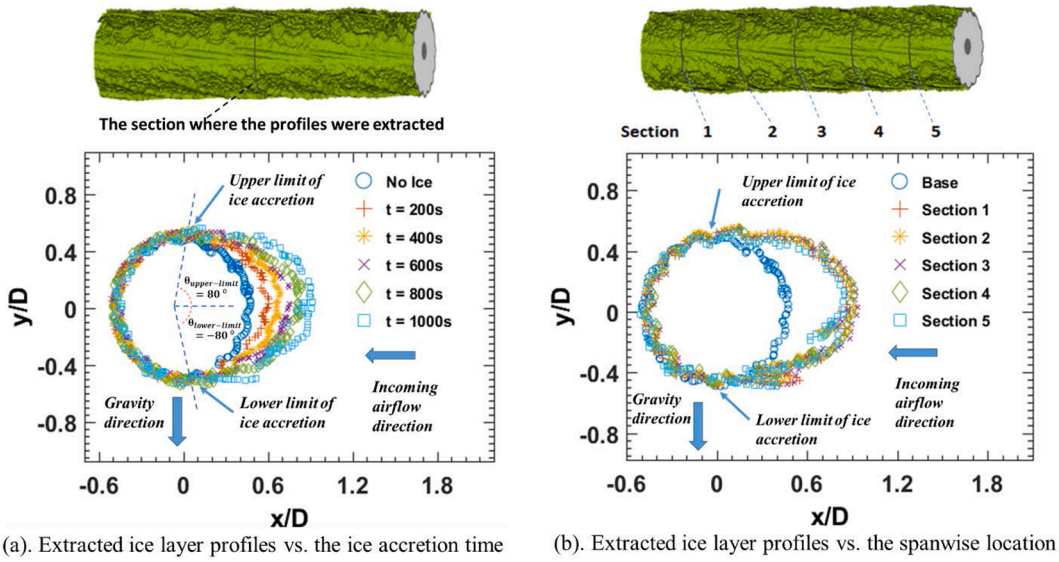

(a). Extracted ice layer profiles vs. the ice accretion time (b). Extracted ice layer profiles vs. the spanwise location

Fig. 4. Outer profiles of the rime ice layer accreted on the ACSR cable model.

progresses, the iced ACSR cable model was observed to have more streamlined outer profile, resulting in continuous reduction of the aerodynamic drag force on the iced cable model, which was confirmed quantitatively from the wind loads measurements to be presented in next section.

As also shown in Fig. 4, the ACSR cable model was horizontally mounted in ISU-IRT with the gravitational force being perpendicular to the incoming airflow. The ice layers accreted on the upper and lower cable surfaces were found to be almost symmetric, suggesting that the gravitational force would not affect the rime icing process. Since the outer profiles of the iced ACSR cable were almost identical at different spanwise sections, it indicates that the rime ice accretion was rather uniform along the spanwise direction. Such experimental observations were quite different from those of glaze icing process to be discussed later, where the accreted ice layer was found to become vary significantly in different spanwise sections. It should be noted that very similar ice accretion characteristics were also observed by Veerakumar et al. [21] on a simplified cable model. It suggested that, since supercooled water droplets would be frozen into solid ice instantly upon impinging onto the cable surface under the rime icing condition, the differences in the surface textures/roughness for the cable models (e.g., the twisted outer strands over the ACSR cable surface versus the smooth surface on the cylindrical cable) had very limited influence on the rime icing process. This is vastly different from the glaze icing process to be discussed in the later section.

The variation characteristics of the resultant wind loads experienced by the iced ACSR cable model were also examined. Fig. 6 presents the temporal evolution of the aerodynamic drag data during the rime icing experiment. It should be noted that, while the duration for the wind load measurements was set to be 1,100 s, the icing process started at 100 s after the force measurements. Based on the measured drag data before turning on the water spray, the mean value of the measured aerodynamic drag, $D_{no\text{-}ice}$, was determined, which is referred as the comparison baseline in examining the effects of ice accretion on the resultant wind loads experienced by the ACSR cable model.

As mentioned in Veerakumar et al. [21], the drag coefficient of a "clean" cylindrical cable (i.e., without any ice accretion) was found to be $C_D = 1.16$ at $Re_D \approx 50{,}000$. Since the twisted outer strands wrapping

around the ACSR cable would be able to function as "turbulators" to promote a faster boundary layer transition of the airflow on the ACSR cable surface, the drag coefficient of the "clean" ACSR cable became slightly smaller with $C_D = 1.05$. The measured drag coefficient of the "clean" ACSR cable agreed well with the numerical simulation result reported in Qi et al. [35].

Since the projected area of the iced ACSR cable may vary substantially due to the ice accretion, especially for the glaze icing cases, instead of using drag coefficient (i.e., the value that depends on the projected area of the iced cable), variations of the icing induced wind loads are presented by normalized drag data (i.e., normalized by the corresponding value of the "clean" cable model, $D_{no\text{-}ice}$). Fig. 5 gives the measured aerodynamic drag during the rime icing process. The aerodynamic drag of the iced ACSR cable model was found to fluctuate significantly both before and after starting the icing process, which is believed to be closely related to the unsteady wake vortex shedding from the cable model as reported by Chen et al.[36]. In the present study, while instantaneous force data were collected at the acquisition rate of 2.0 kHz, moving averaged values of the instantaneous measurements (i.e., averaged at every 5 s) were also given in the plot for comparison.

As described above, since all the impacted supercooled water droplets would be frozen into ice instantly upon impinging onto the cable surface under the rime icing condition, the accreted ice layer was restricted within the droplet direct impinging zone over cable front surface. As icing time progressed, the thickness of the rime ice layer accreted over the cable front surface was found to increase continuously. However, the iced ACSR cable model was found to change its outer profile gradually, becoming more streamline-liked in shape. Thus, the aerodynamic drag was found to decrease gradually with the increasing ice accretion time. Due to the substantial ice accretion over the cable front surface after 1,000 s of the rime icing experiment, the averaged aerodynamic drag of the iced ACSR cable was found to reduce to ~ 85 % of its original value (i.e., without ice accretion). A similar drag reduction trend was also observed in examining the effects of rime ice accretion on the wind loads acting on simplified cylindrical cables [21,31].

The evolution characteristics of the wake flow behind the iced ACSR cable model was also investigated by using a digital PIV system. While instantaneous PIV measurements were conducted at a frame rate of 15 Hz, ensemble-averaged flow field was determined based on 150 frames of instantaneous PIV measurement results (i.e., ensemble-averaged value in every 10 s). Fig. 6 shows the ensemble-averaged airflow fields around the ACSR cable model at six representative time instances before (i.e., $t = 0$ s) and after starting the rime icing experiment (i.e., $t = 200$, 400, 600, 800 and 1000 s, respectively). Simplified shapes of the ice layer accreted on the cable front surface were also plotted for illustration. In comparison to that of the "clean" cable given in Fig. 6(a), the wake flow behind the iced ACSR cable model was found to be more or less constant during the rime icing process or even becoming slightly narrower and shorter as shown in Fig. 6(c) and Fig. 6(d). The narrower and/or smaller wake region behind the iced ACSR cable model implies less momentum deficits in the wake flow, resulting in a less aerodynamic drag for the iced ACSR cable model.

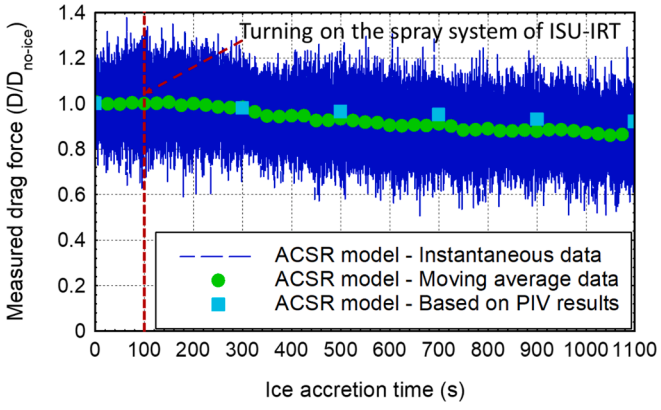

Fig. 5. Measured aerodynamic drag during the rime icing process.

Following up the method given in Hu & Koochesfahani[37], aerodynamic drag acting on a cable model can also be estimated based on PIV measurement results, i.e., calculating the momentum deficits in the cable wake with following equation:

$$C_D = \frac{2}{D}\int_{-H}^{H}\left(\frac{U(y)}{V_\infty}\left(1-\frac{U(y)}{V_\infty}\right)-\frac{U_{rms}(y)^2 - V_{rms}(y)^2}{{V_\infty}^2}+\frac{1}{2}\frac{\left(U_{free-stream}\right)^2}{{V_\infty}^2} - 1\right)dy \quad (1)$$

where V_∞ is the incoming wind speed, $U(y)$ is the ensemble-averaged streamwise velocity profiles of the wake flow. U_{rms} and V_{rms} represent the root-mean-square (i.e., r.m.s.) values of the streamwise and transverse components of the airflow velocity. $U_{free\text{-}stream}$ is the freestream speed of the airflow outside the wake region which is slightly more than the incoming wind speed due to the finite width of test section. The last term on the right-hand side accounts for the corresponding pressure changes in free stream. For the test cases of the present study, the upper and bottom boundary lines of the control volume for the drag calculation were set Y/D = 2.0 and Y/D = -2D. While the upstream boundary line of the control volume was set at X/D = -2.0, the downstream boundary line was set at X/D = 5.0. The estimated aerodynamic drag coefficients based on the PIV measurements were also plotted in Fig. 5 for comparison. While the aerodynamic drag values derived from the PIV measurements agree with the direct force measurement data well in general, the continuous drag reduction trend was also reveal clearly based on the estimated aerodynamic drag data derived from the PIV measurements.

3.2. Characteristics of the icing process over ACSR cable surface under the glaze icing condition

The experimental study was also conducted with the ACSR cable model being exposed to a typical glaze icing condition with the relevant parameters of $T_\infty = -5$ °C, $V_\infty = 20$ m/s and $LWC = 2.0$ g/m^3. Fig. 7 gives acquired images to reveal the glaze icing process on the ACSR cable model. Instead of forming opaque, grainy ice only on the cable front surface under the rime icing condition, the ice layer accreted over the ACSR cable surface under the glaze icing condition were found to be transparent with a glazy appearance. Unfrozen water runback was also observed on the ice accreting cable surface, resulting in a much wider ice coverage on the cable surface with the accreted ice layer reaching to the downstream locations far beyond the droplet direct impinging zone. In comparison to the grainy rime ice structures, the accreted glaze ice structures on the ACSR cable model were found to become much more complex, i.e., forming irregular-shaped ice humps/horns protruding further into the incoming airflow.

Similar as that described in Liu and Hu [27], corresponding to the higher LWC level under the glaze icing condition, a much greater amount of airborne water droplets would impinge onto the cable surface within the same time duration, in comparison to those of rime icing scenario. Thus, the total amount of the released latent heat of fusion would increase significantly due to the solidification of the greater amount of the impacted water mass. However, due to the warmer ambient temperature under the glaze icing condition (i.e., $T_\infty = -5$ °C), convective and/or conductive heat transfer would become much less effective in removing the released latent heat of fusion from the cable surface. As a result, only a portion of the impacted supercooled water droplets would turn into solid ice on the cable surface with the rest of the impacted water droplets remaining in liquid. Driven by the airflow

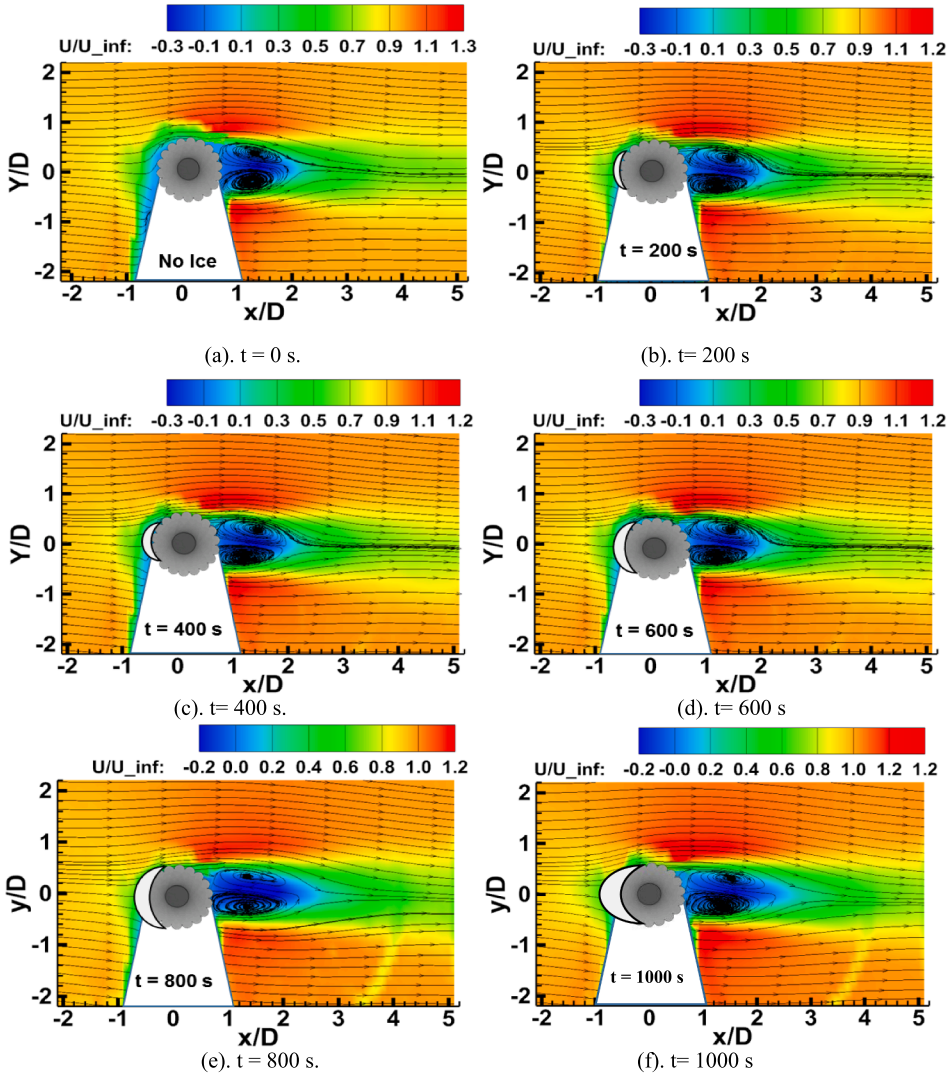

Fig. 6. PIV measurement results during the rime icing process.

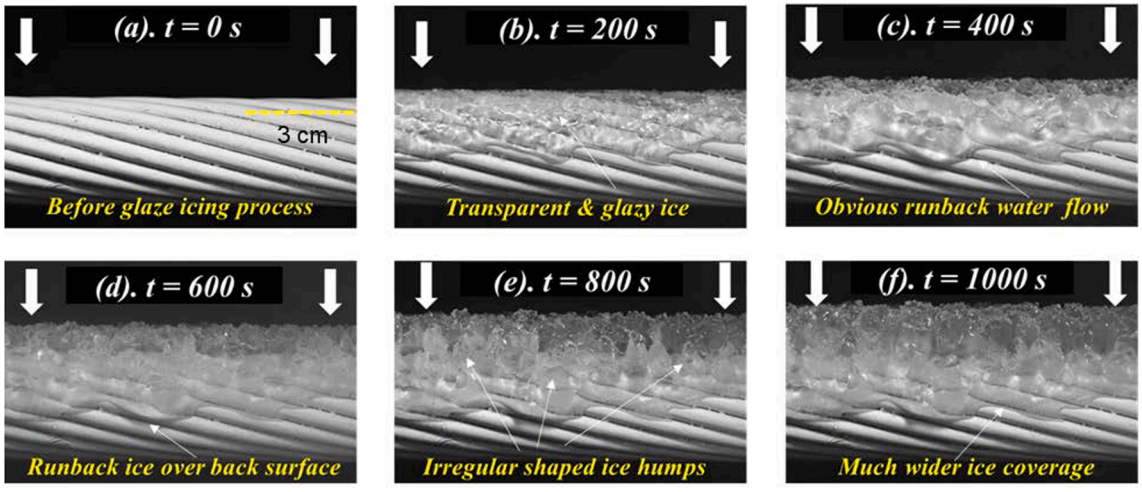

Fig. 7. Acquired images to reveal the glaze icing process on the ACSR cable model.

around the cable surface, the unfrozen water was found to run back over the ice accreting cable surface. However, since the ambient temperature was frozen cold, the runback water would be cooled down continuously, and frozen into ice eventually at further downstream locations (i.e., beyond the direct impinging zone of the airborne water droplets). With more airborne droplets impinging onto the cable surface as the icing

time progresses, the accreted ice layer on the ACSR cable surface grew rapidly, as depicted clearly in Fig. 7.

In comparison to that over the simplified cylindrical cable model as described in Veerakumar et al. [21], the runback process of the unfrozen water flow was found to be changed substantially due to the existence of the twisted outer strands on the ACSR cable model. More specifically, the twisted outer strands wrapping around the ACSR cable model were found to serve as hindrances to delay the runback of the unfrozen water, causing the accumulation of more runback water near the separation points over the cable surface. Thus, the projected aera of the iced ACSR cable model was found to increase rapidly as the time increases. As shown clearly in Fig. 7, the nonlinear interactions among the complex multiple flow system (i.e., runback water flow, frozen-cold incoming airflow, and cable surface) caused the formation of multiple, irregular-shaped ice humps/horns, protruding outward from the cable surface.

The characteristics of the glaze icing process were illustrated more quantitatively from the 3D profiler scanning results given in Fig. 8. The outer profiles of the iced ACSR cable model at five spanwise sections after undergoing 1,000 s of the glaze icing experiment were given in Fig. 9 for a quantitative comparison. It can be seen clearly that much more complicated ice structures (i.e., irregular-shaped ice humps/horns) accreted over the cable surface due to the existence of the runback of the unfrozen water flow over the cable surface. In addition to the formation of the irregular-shaped ice humps/horns, the glaze ice layer accreted on the ACSR cable model was also found to vary greatly along the spanwise direction. This is completely different from the rime icing scenario where a uniform ice layer was observed along the cable span. Furthermore, unliked the rime ice layer being restricted within the droplet direct impinging zone over the cable frontal surface (i.e., between $\theta_{upper\text{-}limit} \approx 80^{\circ}$ and $\theta_{lower\text{-}limit} \approx -80^{\circ}$), the accreted ice layer on the ACSR cable had a much wider coverage under the glaze icing condition. As indicated in Fig. 9, the accreted glaze ice layers were found to extend to a much wider region between $\theta_{lower\text{-}limit} \approx -135^{\circ}$ and $\theta_{upper\text{-}limit} \approx +125^{\circ}$ in general. For occasional cases (e.g., the section #2 given in Fig. 10), the accreted glaze ice layer was found to cover almost entire cable surface.

It should also be pointed out that, under the effects of the gravitational force, the water runback flow on the lower cable surface was more readily to break into rivulets, promoting the formation of irregular-shaped ice humps/horns. It indicates that the glaze icing process would be affected substantially by the gravitational force. Since the irregular-shaped ice humps/horns can further protrude into airflow to intercept more airborne droplets, thereby, to further accelerating the ice accretion process. They would also induce large-scale separations of the incoming airflow from the iced ACSR cable surface. Therefore, the aerodynamic drag of the iced ACSR cable model was found to increase continuously as the ice accretion process progresses, which was confirmed from the aerodynamic force measurement results given in

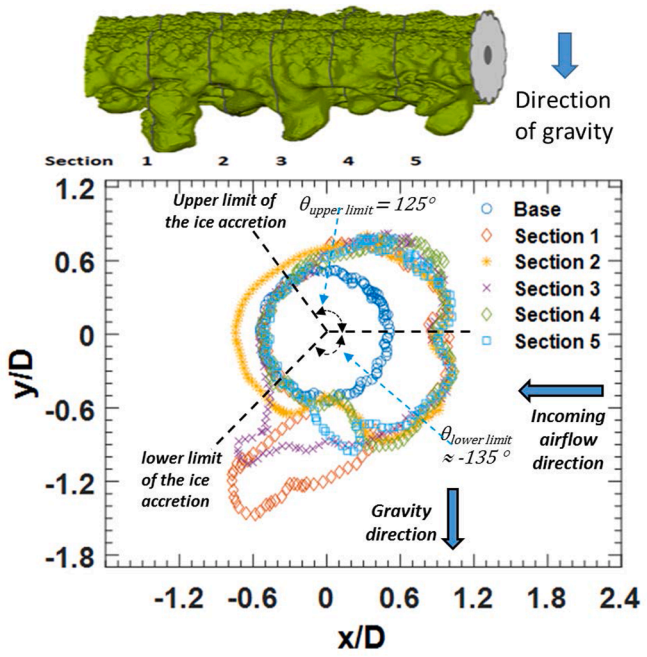

Fig. 9. Outer profiles of the glaze ice layer accreted on the ACSR cable surface.

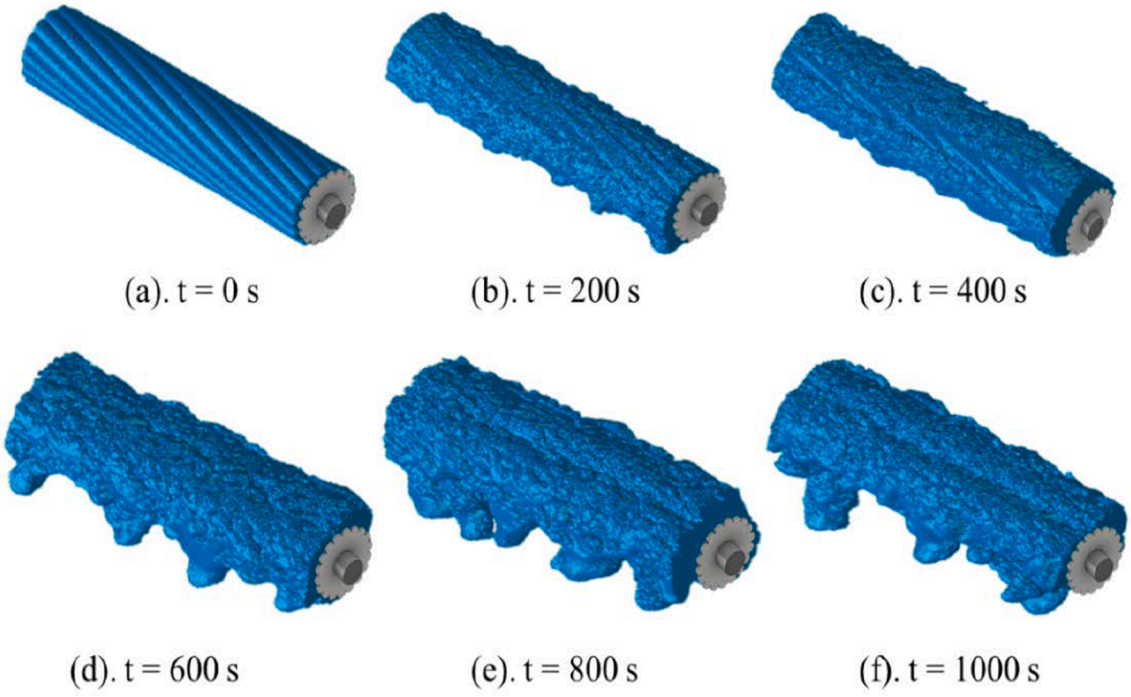

Fig. 8. Measured 3D shapes of the iced ACSR cable during glaze icing process.

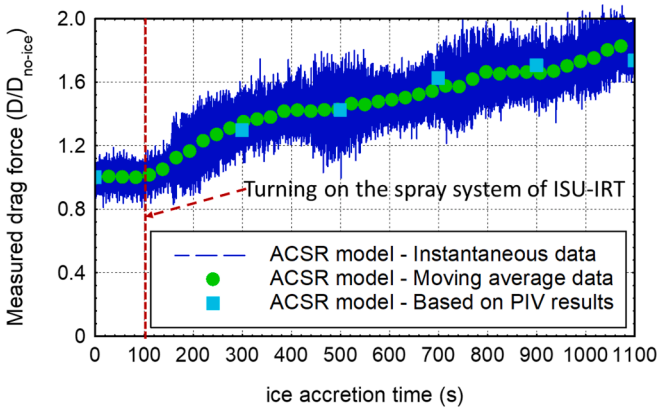

Fig. 10. Measured aerodynamic drag during the glaze icing process.

Fig. 10.

As shown quantitatively in Fig. 10, the temporal evolution of the aerodynamic drag experienced by the ACSR cable model during the glaze icing process became significantly different from those of the rime icing process. Instead of exhibiting a continuous drag reduction trend under the rime icing condition, the aerodynamic drag was found to increase monotonically with the ice accretion time under the glaze icing condition. This can be explained by the fact that, since only a portion of the impinged supercooled water droplets would to be frozen into solid ice instantly under the glaze icing condition, the wind-driven runback of the unfrozen water mass over the cable surface would cause the formation of a transparent, glazy ice layer to cover a much wider area over the cable surface. As the time progresses, the thickness of the accreted glaze ice layer was found to increase continuously, causing the projected area of the iced ACSR cable model growing subsequently. Hence, the aerodynamic drag values were found to become greater with the increasing ice accretion time under the glaze icing condition. Furthermore, the formation of irregular-shaped glaze ice humps/horns on the cable surface would also induce large-scale airflow separation, leading to a greater aerodynamic drag for the iced ACSR cable. While a similar drag increasing feature was also reported by Veerakumar [21] with a simplified cylindrical cable being exposed to the same testing condition, the aerodynamic drag of the iced ACSR cable was found to have a much

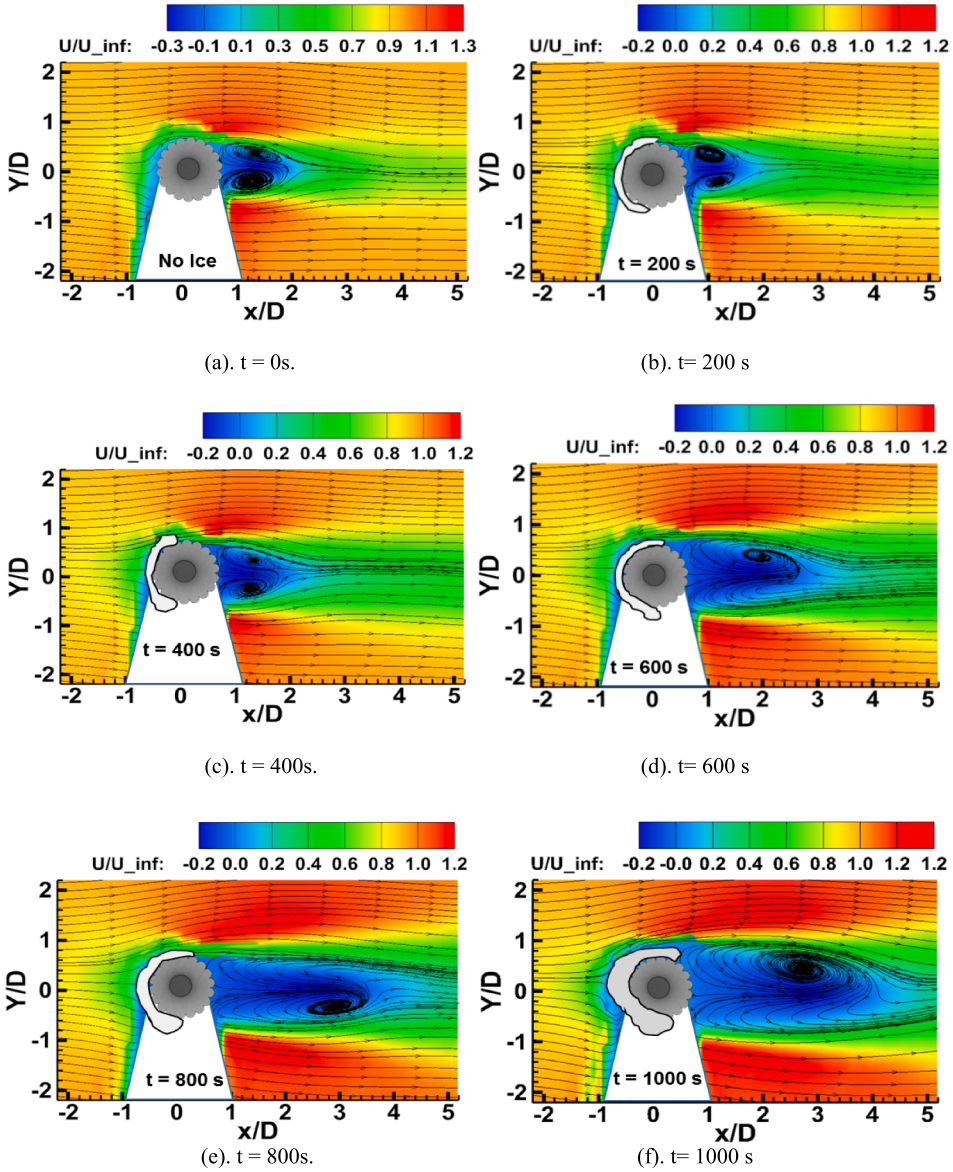

(a). t = 0s. (b). t= 200 s

(c). t = 400s. (d). t= 600 s

(e). t = 800s. (f). t= 1000 s

Fig. 11. PIV measurement results during the glaze ice accreting process.

faster increase rate. For example, while the aerodynamic drag acting on the iced cylindrical cable increased 45 % after undergoing 1,000 s of the glaze icing experiment [21], the corresponding value was found to became 80 % for the iced ACSR cable. It confirms again that the differences in the textures/roughness over the cable surfaces (i.e., twisted outer strands for the ACSR cable model vs. smooth surface for the simplified cylindrical cable model) would influence the glaze icing process substantially.

Fig. 11 gives typical PIV results to quantify the wake flow behind the ACSR model during the glaze icing process. In comparison to those behind the "clean" ACSR cable, the wake flow characteristics were found to vary significantly due to the glaze ice accretion. As the ice accretion time increases, the glaze ice layer accreted over the ACSR cable surface was found to grow rapidly, causing a substantially greater projected area of the iced ACSR cable in the airflow direction. As a result, the recirculation zone behind the iced ACSR cable became wider and longer. The irregular-shaped ice humps/horns over the cable surface would also contribute to the formation of the bigger and wider recirculation region behind the iced ACSR model. The longer and wider recirculation zone imply greater momentum deficits in the wake flow, resulting in a larger aerodynamic drag experienced by the iced ACSR cable model as revealed quantitatively from the aerodynamic force measurement results given in Fig. 10.

Based on the PIV measurement results given in Fig. 12, the aerodynamic drag of the ACSR cable model can also be estimated with the formula given in equation (1). The estimated drag coefficients based on the PIV measurements were also given in Fig. 10 for comparison. It can be seen clearly that the estimated aerodynamic drag data derived from the PIV results agreed reasonably well with the directly measured drag data. The increasing drag trend for the iced ACSR cable due to glaze ice accretion was also confirmed from the estimated drag data based on the PIV results.

3.3. Accumulated ice mass on ACSR cable under different icing conditions

Based on the 3D profiler scanning measurement results under different icing conditions, the total volume of the ice layers accreted on the ACSR cable surface can be determined quantitatively. According to Liu et al. [38], while the density of glaze ice is about 900 kg/m^3, and the corresponding value is 880 kg/m^3 for typical rime ice. Hence, the total mass of the ice structures accumulated on the ACSR cable surface can also be estimated quantitatively.

Fig. 12 presents the accumulated ice mass on the ACSR cable model under different icing conditions in the term of kilogram per meter in cable span (i.e., Kg/m). The measured ice mass accreted on a simplified cylindrical cable model under the same icing conditions reported in Veerakumar et al.[21] are also given in the plot for comparison. While the accumulated ice mass would grow continuously with the icing time

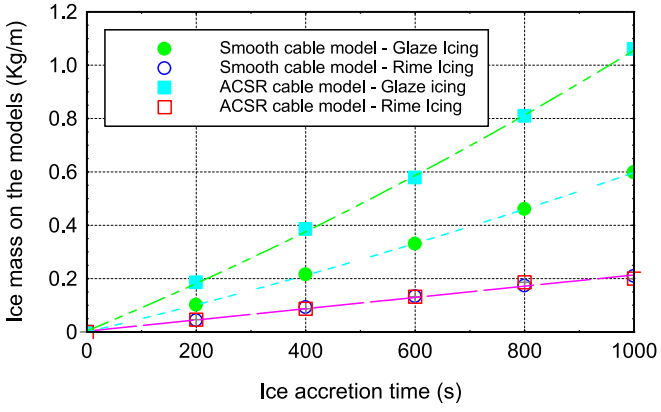

Fig. 12. Time evolution of the ice mass accreted on the ACSR cable model.

as expected, the growth rates under different icing conditions were found to vary substantially. Under the rime icing condition, while the measured values of the accumulated ice mass on the two compared cable surface were found to be almost identical, the growth profile was fitted well with a linear function. It indicates again that, with the same nominal cable diameter, the differences in the textures/roughness over the cable surface (i.e., rough twisted outer strands for the ACSR cable vs. smooth surface for the cylindrical cable) were found to have almost no effect on the rime icing process.

However, the situations were found to become completely difference under the glaze icing condition. The ice mass accumulated on the ACSR cable surface was found to grow much faster than that on the simplified cylindrical model. For example, the accumulated ice mass on both the ACSR cable and simplified cylindrical cable models was found to be about 0.20 kg/m after 1,000 s of the rime icing experiment with $LWC =$ 1.0 g/m^3. In comparison, with the glaze icing experiments being performing with $LWC = 2.0$ g/m^3 (i.e., 2.0 times of the rime icing case), the accumulated ice mass on the cylindrical cable was found to increase to 0.59 kg/m (i.e., ~3.0 times of the rime icing case) after undergoing 1,000 s of the glaze icing experiment. The corresponding value became 1.06 kg/m (i.e., > 5.0 times of the rime icing value) on the ACSR cable surface. It indicates again that the differences in the cable surface textures/roughness would affect the glaze icing process substantially.

The experimental results are closely correlated to the different icing characteristics over the cable surfaces. As described earlier, since all the supercooled water droplets would turn into solid ice instantly upon impinging onto the cable surface under the rime icing condition, accreted rime ice structures were found to be restrained within the direct impingement zone of the droplets over the cable frontal surface. Since rime icing process would depend mainly on the water collection efficiency distribution over the cable surface (i.e., associated with the shape of the test model) [27], it is almost independent to the surface textures/roughness of the test model. As aforementioned, while the rime ice accreted over the cable front surface would make the iced cable model becoming more "streamline-liked" in shape, the projected area of the iced cable model was almost unchanged during the rime icing process. As a result, the accumulated ice mass on the cable surface would grow linearly as the ice accretion time progresses.

However, since only a portion of the impacted supercooled water droplets could be frozen into solid ice immediately under the glaze icing condition, the rest of the impacted water droplets would remain in liquid over the cable surface. Driven by the incoming airflow, the unfrozen water mass was found to run back freely over the cable surface to transport the water mass from the cable front surface to further downstream locations, causing the formation of runback ice in the downstream regions beyond the direct impinging zone of the airborne droplets. As the time increases, the glaze ice layer accreted over the cable surface was found to grow rapidly, causing the continuous increase in the projected area of the iced cable. Hence, the airborne water droplets would be intercepted by the cable model over a much wider range, resulting in the faster and nonlinear growth of the ice mass accumulated on the cable surface. While such processes were found to take place over both the cylindrical and ACSR cable surfaces, additional effects of the twisted strands on the runback of the unfrozen water over the ACSR cable surface were found to cause substantial changes to the glaze icing process.

As described in Hansman & Turnock [39], the behavior of unfrozen water flowing over an accreting ice surface would greatly influence the resultant shapes of the glaze ice structures on the model surface. Due to the significant differences in the surface textures/roughness, the water runback characteristics on the rather rough ACSR cable surface became substantially different from that on the smooth surface of the simplified cylindrical cable. Even though the incoming airflow was kept same, unfrozen water would flow much more swiftly over the smooth surface of the cylindrical cable model. Due to existence of the twisted outer strands over the ACSR cable surface, runback process of the unfrozen

water was slow down substantially with the water being easily trapped into the gaps between adjacent strands, causing thicker ice layers accreted near the separation points of the ACSR cable model. As a result, the iced ACSR cable model was found to have a greater projected area, in comparison to the cylindrical cable case. This would create a cascading effect to enable more airborne water droplets being intercepted by the iced ACSR cable model. Therefore, the accumulated ice mass on the ACSR cable surface grew much faster than that over the smooth surface of the simplified cylindrical cable when exposed under the same glaze icing condition.

4. Conclusion

An experimental campaign was performed to study the dynamic icing process on an ACSR power cable model with twisted outer strands and examine the variation characteristics of the resultant wind loads experienced by the ACSR cable induced by ice accretion. The icing experiments were performed in an Icing Research Tunnel (i.e., ISU-IRT) with an ACSR cable model mounted horizontally in the test section under two types of atmospheric icing conditions (i.e., dry rime and wet glaze icing) usually experienced by power cables. During the icing experiments, while the dynamic icing process over the cable surface was recorded by using a high-speed digital imaging system, the three-dimensional (3D) shapes of the ice structures accreted on the cable model was quantified by using a 3D profiler scanning system. The evolution of the wake flow behind the ACSR cable model was characterized by using a high-resolution Particle Image Velocimetry (PIV) system. The resultant wind loads acting on the iced cable model was also measured by using high-sensitive force/moment transducers.

Under the rime icing condition with relatively low Liquid Water Content (i.e., $LWC = 1.0$ g/m^3) and low ambient temperature (i.e., $T_\infty = -15.0$ °C), the airborne, supercooled water droplets were found to turn into solid ice instantly after impacting onto the cable surface. While the ice accretion was found to be restricted within the direct impinging zone of the airborne water droplets over the front surface of the ACSR cable model (i.e., within the region between the azimuthal angles of $\theta \approx \pm 80°$), the accreted ice layer was observed to be opaque and milk white with grainy appearance. As the icing time progresses, while the ice layer accreted over the cable front surface increased monotonically, the iced ACSR cable was found to become more "streamline-liked" in shape. While the PIV measurement results revealed that wake region behind the iced ACSR cable model was found to stay almost unchanged throughout the entire rime icing process, the resultant aerodynamic drag decreased gradually as the icing experiment progresses. The aerodynamic drag of the iced ACSR cable model was reduced by ~ 15 % after 1,000 s of the rime icing experiments. With the projected area of the iced ACSR cable remaining essentially unchanged during the rime icing process, the ice mass accumulated on the ACSR cable surface increased almost linearly with the ice accretion time. In comparison that over the smooth surface of simplified cylindric cable model, the rime icing process was found to be almost unaffected by the twisted outer strands over the ACSR cable surface. The gravitational force was also found to have almost no effects on rime icing process, leading to a nearly symmetric ice accretion over the upper and lower cable surfaces.

The glaze icing process over the ACSR cable surface was found to be much more complicated. Due to the warmer ambient temperature (i.e., $T_\infty = -5$ °C) and the higher LWC level (i.e., $LWC = 2.0$ g/m^3) the convective/conductive heat transfer became much less effective to swiftly dissipate all the released latent heat of fusion associated with the solidification of the greater amount of the impacted water droplets. As a result, only a portion of the supercooled water droplets froze into solid ice immediately upon impinging onto the cable surface with the rest of the impacted water droplets staying in liquid. Driven by the incoming airflow over the cable surface, the unfrozen water would run freely back over the ice accreting cable surface. The runback water flow was cooled down continuously and frozen into runback ice eventually at further downstream locations, causing a much wider ice coverage over the cable surface. The accreted ice layer was found to be transparent with glazy appearance. As the ice accretion time increases, the thickness of the accreted ice layer accreted was found to increase rapidly, causing a continuously enlarged projected area of the iced cable model along the incoming airflow direction. Hence, while the recirculation zone behind the iced ACSR cable became longer and wider, the aerodynamic drag experienced by the iced ACSR cable was found to increase continuously, i.e., becoming 180 % greater after undergoing 1,000 s of the glaze icing experiment. Corresponding to the greater projected area, the iced ACSR cable was able to intercept more airborne water droplets, resulting in a much faster growth of the accumulated ice mass on the ACSR cable surface. While the LWC level of the glaze icing case was increased to 2.0 times of the rime icing case, the accumulated ice mass on the ACSR cable became over 5.0 times greater after undergoing 1,000 s of the glaze icing experiments.

The behavior the unfrozen water runback over the cable surface was found to affect the glaze icing process significantly. Due to the gravity effects, more unfrozen water accumulated over the lower surface of the ACSR cable, in comparison to that over the upper surface. It caused a more readily formation of irregular-shaped glaze ice structures (i.e., ice horns/humps) over the lower cable surface. The runback process of the unfrozen water was found to slow down substantially due to the existence of the twisted outer strands over the ACSR cable surface, in comparison to those over smooth surfaces of simplified cylindric cables. Furthermore, the runback water was more readily trapped into the gaps between adjacent strands, causing a faster growing projected area of the iced cable model in respected to the incoming airflow. Coupled with the effects of gravitational force, more complex ice humps/horns were found to form over the ACSR cable surface, which could protrude further into the incoming airflow to intercept more airborne water droplets to further accelerate the ice accretion. As a result, due to the existence of the twisted outer strands over the ACSR cable surface, the ice mass accumulated on the ACSR cable surface was found to grow much faster than those over the smooth surfaces of the simplified cylindrical cables when exposed to the same glaze icing condition.

CRediT authorship contribution statement

Ramsankar Veerakumar: Data curation, Formal analysis, Investigation, Writing – original draft. **Linchuan Tian:** Data curation, Formal analysis, Investigation. **Haiyang Hu:** Data curation, Formal analysis, Investigation. **Yang Liu:** Data curation, Formal analysis, Investigation. **Hui Hu:** Conceptualization, Methodology, Formal analysis, Writing – review & editing, Funding acquisition, Project administration, Supervision.

Declaration of Competing Interest

The authors declare that they have no known competing financial interests or personal relationships that could have appeared to influence the work reported in this paper.

Data availability

Data will be made available on request.

Acknowledgments

The authors would like to acknowledge the support from Iowa Energy Center (IEC) under the IEC competitive grant #31250. The research is also partially funded by National Science Foundation (NSF) under award numbers of CMMI-1824840 and CBET-1916380.

References

[1] S. Gupta, T.J. Wipf, F. Fanous, M. Baenziger, Y.H. Hahm, Structural Failure Analysis of 345 KV Transmission Line, IEEE Trans. Power Delivery 9 (2) (1994) 894–903, https://doi.org/10.1109/61.296272.

[2] N.D. Mulherin, Atmospheric Icing and Communication Tower Failure in the United States, Cold Reg. Sci. Technol. 27 (2) (1998) 91–104, https://doi.org/10.1016/S0165-232X(97)00025-6.

[3] T. Wagner, Atmospheric Icing of Transmission Line Conductor Bundles, in: *Proceedings of the COMSOL Conference 2008 Hannover*, No. September, 2008.

[4] R. Hann, R.J. Hearst, L.R. Sætran, T. Bracchi, Experimental and Numerical Icing Penalties of an S826 Airfoil at Low Reynolds Numbers, Aerospace 7 (4) (2020) 46, https://doi.org/10.3390/AEROSPACE7040046.

[5] M. Farzaneh, Ice Accretions on High-Voltage Conductors and Insulators and Related Phenomena, Philos. Trans. R. Soc. A Math. Phys. Eng. Sci. 358 (1776) (2000) 2971–3005, https://doi.org/10.1098/rsta.2000.0692.

[6] J.C. Pohlman, P. Landers, Present State of the Art of Transmission Line Icing, in: *IEEE Transactions on Power Apparatus and Systems*, Vol. PAS-1, No. 8, 1982, pp. 2443–2450.

[7] M. Farzaneh, (Ed). *Atmospheric Icing of Power Networks*. Springer Science & Business Media, 2008., 2008.

[8] G. Fu, L. Wang, Z. Guan, X. Meng, Study on the Prevention of Conductor Ice-Shedding by Interphase Spacer. 2009.

[9] J. Hrabovský, R. Gogola, J. Murín, T. Sedlár, Modeling of Ice-Shedding from ACSR Power Line, Strojnícky casopis – J. Mech. Eng. 67 (1) (2017) 45–54, https://doi.org/10.1515/scjme-2017-0005.

[10] K. Ji, X. Rui, L. Li, A. Leblond, G. McClure, A Novel Ice-Shedding Model for Overhead Power Line Conductors with the Consideration of Adhesive/Cohesive Forces, Comput. Struct. 157 (2015) 153–164, https://doi.org/10.1016/j.compstruc.2015.05.014.

[11] H.H. Koss, H. Gjelstrup, C.T. Georgakis, Experimental Study of Ice Accretion on Circular Cylinders at Moderate Low Temperatures, J. Wind Eng. Ind. Aerodyn. 104–106 (2012) 540–546, https://doi.org/10.1016/J.JWEIA.2012.03.024.

[12] H. Qing, Z. Jian, D. Mengyan, D. Dongmei, L. Makkonen, M. Tiihonen, Rime Icing on Bundled Conductors, Cold Reg. Sci. Technol. 158 (2019) 230–236, https://doi.org/10.1016/J.COLDREGIONS.2018.08.027.

[13] L. Makkonen, Modeling Power Line Icing in Freezing Precipitation, Atmos. Res. 46 (1–2) (1998) 131–142, https://doi.org/10.1016/S0169-8095(97)00056-2.

[14] L. Makkonen, B. Wichura, Simulating Wet Snow Loads on Power Line Cables by a Simple Model, Cold Reg. Sci. Technol. 61 (2–3) (2010) 73–81, https://doi.org/10.1016/J.COLDREGIONS.2010.01.008.

[15] K. Szilder, Theoretical and Experimental Study of Ice Accretion Due to Freezing Rain on an Inclined Cylinder, Cold Reg. Sci. Technol. 150 (2018) 25–34, https://doi.org/10.1016/J.COLDREGIONS.2018.02.004.

[16] A. Zarnani, P. Musilek, X. Shi, X. Ke, H. He, R. Greiner, Learning to Predict Ice Accretion on Electric Power Lines, Eng. Appl. Artif. Intel. 25 (3) (2012) 609–617, https://doi.org/10.1016/j.engappai.2011.11.004.

[17] L. Gao, Y. Liu, W. Zhou, H. Hu, An Experimental Study on the Aerodynamic Performance Degradation of a Wind Turbine Blade Model Induced by Ice Accretion Process, Renew. Energy 133 (2019) 663–675, https://doi.org/10.1016/J.RENENE.2018.10.032.

[18] L. Li, Y. Liu, Z. Zhang, H. Hu, Effects of Thermal Conductivity of Airframe Substrate on the Dynamic Ice Accretion Process Pertinent to UAS Inflight Icing Phenomena, Int. J. Heat Mass Transf. 131 (2019) 1184–1195, https://doi.org/10.1016/J.IJHEATMASSTRANSFER.2018.11.132.

[19] L. Gao, R. Veerakumar, Y. Liu, H. Hu, "Quantification of 3D Ice Structures Accreted on a Wind Turbine Airfoil Model,." 2019.

[20] Y. Liu, W. Chen, Y. Peng, H. Hu, An Experimental Study on the Dynamic Ice Accretion Processes on Bridge Cables with Different Surface Modifications, J. Wind Eng. Ind. Aerodyn. 190 (April) (2019) 218–229, https://doi.org/10.1016/j.jweia.2019.05.007.

[21] R. Veerakumar, L. Gao, Y. Liu, H. Hu, Dynamic Ice Accretion Process and Its Effects on the Aerodynamic Drag Characteristics of a Power Transmission Cable Model, Cold Reg. Sci. Technol. 169 (2020), 102908, https://doi.org/10.1016/j.coldregions.2019.102908.

[22] J. Li, B. Du, J. Su, H. Liang, Y. Liu, Surface Layer Fluorination-Modulated Space Charge Behaviors in HVDC Cable Accessory, Polymers 10 (5) (2018) 500, https://doi.org/10.3390/polym10050500.

[23] Y. Liu, L. Li, H. Li, H. Hu, An Experimental Study of Surface Wettability Effects on Dynamic Ice Accretion Process over an UAS Propeller Model, Aerosp. Sci. Technol. 73 (2) (2018) 164–172, https://doi.org/10.1016/j.ast.2017.12.003.

[24] A. Work, Y. Lian, A Critical Review of the Measurement of Ice Adhesion to Solid Substrates, in: *Progress in Aerospace Sciences*, No. March, 2018, pp. 1–26. Doi: 10.1016/j.paerosci.2018.03.001.

[25] O. Parent, A. Ilinca, Anti-Icing and de-Icing Techniques for Wind Turbines: Critical Review, Cold Reg. Sci. Technol. 65 (1) (2011) 88–96, https://doi.org/10.1016/j.coldregions.2010.01.005.

[26] R. Waldman, H. Hu, An Experimental Investigation of the Effects of Surface Hydrophicity on the Ice Accretion Process over a NACA0012 Airfoil, J. Aircr. submitted (2016).

[27] Y. Liu, H. Hu, An Experimental Investigation on the Unsteady Heat Transfer Process over an Ice Accreting Airfoil Surface, Int. J. Heat Mass Transf. 122 (2018) 707–718.

[28] D. Mangini, C. Antonini, M. Marengo, A. Amirfazli, Runback Ice Formation Mechanism on Hydrophilic and Superhydrophobic Surfaces, Cold Reg. Sci. Technol. 109 (2015) 53–60, https://doi.org/10.1016/j.coldregions.2014.09.012.

[29] K. Zhang, T. Wei, H. Hu, An Experimental Investigation on the Surface Water Transport Process over an Airfoil by Using a Digital Image Projection Technique, Exp. Fluids 56 (9) (2015) 173, https://doi.org/10.1007/s00348-015-2046-z.

[30] L. Gao, R. Veerakumar, Y. Liu, H. Hu, Quantification of the 3D Shapes of the Ice Structures Accreted on a Wind Turbine Airfoil Model, J. Vis. 22 (4) (2019) 661–667, https://doi.org/10.1007/s12650-019-00567-4.

[31] Y. Peng, R. Veerakumar, Z. Zhang, H. Hu, Y. Liu, X. He, H. Hu, An Experimental Study on Mitigating Dynamic Ice Accretion Process on Bridge Cables with a Superhydrophobic Coating, Exp. Therm Fluid Sci. 132 (2022), 110573, https://doi.org/10.1016/J.EXPTHERMFLUSCI.2021.110573.

[32] Z. Zhang, Y. Liu, H. Hu, Effects of Chamber Pressure on the Kinematic Characteristics of Spray Flows Exhausted from an Airblast Atomizer, Exp. Therm Fluid Sci. 130 (2022), 110514, https://doi.org/10.1016/J.EXPTHERMFLUSCI.2021.110514.

[33] D.N. Anderson, J.-C. Tsao, Overview of Icing Physics Relevant to Scaling, NASA/CR—2005-213851 No. 724 (2005), https://doi.org/10.4271/2003-01-2130.

[34] M. Pourbagian, W.G. Habashi, Surrogate-Based Optimization of Electrothermal Wing Anti-Icing Systems, J. Aircr. 50 (5) (2013) 1555–1563, https://doi.org/10.2514/1.C032072.

[35] L. Qi, M. Wang, G. Xu, Z. Wang, Numerical Simulation of Aerodynamic Forces of ACSR Conductor, in: *Proceedings of the 2015 International conference on Applied Science and Engineering Innovation*, Vol. 12, 2015. Doi: 10.2991/ASEI-15.2015.375.

[36] W.-L. Chen, H. Li, H. Hu, An Experimental Study on a Suction Flow Control Method to Reduce the Unsteadiness of the Wind Loads Acting on a Circular Cylinder, Exp. Fluids 55 (4) (2014) 1707, https://doi.org/10.1007/s00348-014-1707-7.

[37] H. Hu, M.M. Koochesfahani, Thermal Effects on the Wake of a Heated Circular Cylinder Operating in Mixed Convection Regime, J. Fluid Mech. 685 (2011) 235–270, https://doi.org/10.1017/jfm.2011.313.

[38] Y. Liu, L.J. Bond, H. Hu, Ultrasonic-Attenuation-Based Technique for Ice Characterization Pertinent to Aircraft Icing Phenomena, AIAA J. (2017) 1–8, https://doi.org/10.2514/1.J055500.

[39] R.J. Hansman, S.R. Turnock, Investigation of Surface Water Behavior during Glaze Ice Accretion, J. Aircr. 26 (2) (1989) 140–147.